The Brugada syndrome associated gene *WT1* impacts on *SCN5A* expression and cardiac conduction

E. Madelief J. Marsman*[1], Joost A. Offerhaus*[1,2], Isabella Mengarelli[1], Leander Beekman[1,2], Lisanne M.W. Wilde[1], Simona Casini[1], Marie-José Goumans[5], Arie O. Verkerk[1,3], Sean J. Jurgens[1], Arthur A.M. Wilde[1,2], Bastiaan J. Boukens[4], Carol Ann Remme[1], Connie R. Bezzina*[1], Fernanda M. Bosada*[1].

* Equal contribution

[1] Department of Experimental Cardiology, Amsterdam Cardiovascular Sciences, Amsterdam University Medical Centers, University of Amsterdam, Amsterdam, The Netherlands.

[2] Department of Clinical Cardiology, Heart Center, Amsterdam Cardiovascular Sciences, Amsterdam University Medical Centers, University of Amsterdam, Amsterdam, The Netherlands.

[3] Department of Medical Biology, Amsterdam University Medical Centers, University of Amsterdam, Amsterdam, The Netherlands.

[4] Department of Physiology, Cardiovascular Research Institute Maastricht University Maastricht Maastricht, The Netherlands.

[5] Department of Cell and Chemical Biology, Leiden University Medical Center, Leiden, Netherlands.

Abstract

Brugada syndrome (BrS) is an inherited cardiac arrhythmic disorder caused by conduction slowing primarily affecting the right ventricular (RV) outflow tract (RVOT). A recent genome-wide association study (GWAS) implicated a genomic region in chromosome 11, overlapping the transcription factor *WT1*, in BrS susceptibility. Here, we investigated the role of *WT1* on cardiac conduction using a heterozygous knockout mouse model (*Wt1*$^{+/-}$). Transcriptomic analysis revealed increased *Scn5a* expression predominantly in *Wt1*$^{+/-}$ cardiomyocytes of the (sub)epicardium of the RV and RVOT without any changes in electrical properties. To unmask an effect on cardiac conduction, we performed optical mapping in a severely challenged setting offered by *Scn5a* haploinsufficiency, ageing, and exposure to the sodium channel blocker ajmaline and found that diminished *Wt1* improved the observed slowed conduction. Examination of human single-nuclei cardiac datasets indicated a strong negative correlation between *WT1* and *SCN5A* expression. In line with this observation, cardiac samples from patients with mutations in *SCN5A* showed increased WT1 protein abundance in histological sections, suggesting that increased *WT1*, and not loss, is associated with BrS pathophysiology. By deleting the mouse orthologue of a BrS-associated noncoding region (RE) harboring a candidate regulatory element, we established that this RE controls expression of *Wt1* specifically in the (sub)epicardium of the RV. Lastly, transient overexpression of *WT1* in hiPSC-derived cardiomyocytes resulted in reduced sodium current density. Our study therefore identifies the transcription factor *WT1* as a novel contributor to the pathophysiology of BrS, at least in part, through *SCN5A*.

Introduction

Brugada Syndrome (BrS) is a heritable cardiac arrhythmia associated with increased risk of sudden cardiac death in young adults [1–3]. The pathophysiological mechanisms underlying BrS remain incompletely understood, hindering development of much needed strategies for risk stratification for life-threatening arrhythmic events and therapy. A long-standing hypothesis revolves around the slowing of conduction of the cardiac electrical impulse, to which the right ventricle (RV) and (epicardial) right ventricular outflow tract (RVOT) are particularly sensitive [4] likely due to their lower conduction reserve [5] and propensity for fibrosis formation [6]. This premise is supported by the fact that rare pathogenic loss-of-function variants in *SCN5A*, encoding the cardiac sodium channel ($Na_V1.5$), a critical determinant of cardiac conduction, are found in ~20% of BrS patients [7,8] although the vast majority of cases remain genetically elusive [9]. BrS was, until recently, considered a monogenic disease. However, major advances in genetics have uncovered a more complex (polygenic) inheritance. Genome-wide association studies (GWAS) have identified 12 genetic loci harboring common variants associated with increased risk for BrS [10,11]. The majority of these disease risk-associated variants are found in noncoding genomic regions, and are presumed to alter the functionality of regulatory elements (REs) [12–14], which in turn lead to changes in gene expression. The disease-associated loci harbor *SCN5A*, genes that converge at $Na_V1.5$ regulation via transcriptional or post transcriptional mechanisms [10,15,16], as well as transcription factors (TFs) that may play a role in patterning of ion channel expression across the ventricular wall [15]. This supports the notion that diminished $Na_V1.5$ function is a central mechanism in BrS pathophysiology. Studies aimed at reliably identifying genes contributing to disease, and exploring how variants affect their expression, are crucial to understand BrS pathophysiology.

68 GWAS identified a genomic region enriched with noncoding BrS-associated variants in
69 chromosome 11, directly upstream of *WT1* (Wilm's Tumor 1) [10]. This transcription factor is
70 expressed during development and is known to drive epithelial-to-mesenchymal transition
71 (EMT) to form a population of multipotent epicardial-derived cells [17,18]. Endogenous *Wt1*
72 expression can be found in cardiomyocytes during development [19–22]; while it diminishes
73 postnatally, it can become re-expressed upon injury [23–26] or in the setting of disease [27–29]. More
74 recently, two studies demonstrated that conditional ablation of *Wt1* in cardiomyocytes during
75 development or postnatally results in morphological abnormalities and *in vivo*
76 electrophysiological changes [22,30]. However, the possible impact of WT1 on ion channel
77 expression and function has yet to be explored. Here, we establish a clear association between
78 by using a heterozygous knockout mouse model (*Wt1*$^{+/-}$), and overexpressing this TF and BrS,
79 while demonstrating the direction of change in expression that may be present in patients.
80 transcription factor in human induced pluripotent stem cell (hiPSC)-derived cardiomyocytes.

81

82
83 **Results**

84 ***Wt1*$^{+/-}$ RV cardiomyocytes show altered ion channel expression without detectable**
85 **electrophysiological changes**

86 Since GWAS indicated an association with variants directly overlapping *WT1* [10], we
87 studied the role of this transcription factor using a heterozygous null mouse model (*Wt1*$^{+/-}$). To
88 investigate how reduced *Wt1* affects the transcriptomes of cardiomyocytes, we performed RNA-
89 sequencing on PCM1-positive nuclei from RV/RVOT tissue of aged *Wt1*$^{+/-}$ (n=4; 15+ months)
90 mice and age-matched controls (n=4) (Figure 1A). Aged mice were studied in order to resemble
91 the age at which clinical BrS features become apparent in patients. Among 10722 transcripts
92 detected (>10 averaged normalized reads), 466 were upregulated and 405 downregulated in
93 *Wt1*$^{+/-}$ cardiomyocyte nuclei (Figure 1B). Notably, *Wt1* transcripts were almost undetectable in
94 our cardiomyocyte-enriched samples (Supplemental Table 1). Gene ontology term analysis
95 using PANTHER [31] identified biological processes including development (*Rbm20*, *Mef2d*,
96 *Tcf7l2, Sox6*), cardiac muscle contraction (*Cacna1c*, *Ryr2*, *Slc9a1, Myh7b*), and cell motility
97 (*Actg1*, *Ctnna1*, *Cdh13, Sema6d*) associated with upregulated genes in *Wt1*$^{+/-}$. Cellular
98 respiration (*Mtch2*, *Cox7b*, *Mdh1, Dld*), muscle tissue development (*Tgfb2*, *Myoz2*, *Hand2,*
99 *Gata6*), and intracellular transport (*Dnm1l*, *Mtx2, Calm1/2/3*) were associated with the
100 downregulated gene set (Figure 1C). Strikingly, we found increased *Scn5a* (L2FC 0.2333, p-
101 adj=0.0124) and various deregulated genes involved in cellular electrophysiology in *Wt1*$^{+/-}$
102 cardiomyocytes (Figure 1B, D).

103 Given the well-established ventricular transmural ion channel expression gradient for
104 normal conduction [15,32], we tested the impact of diminished *Wt1* in the ventricular
105 (sub)endocardial and (sub)epicardial sides of the ventricular wall on *Scn5a* levels by RT-qPCR.
106 As expected, we observed that in control hearts, *Scn5a* expression was higher in the

107 (sub)endocardial side (Figure 1E), while *Wt1* showed a clear tendency to higher expression in
108 the (sub)epicardial side (Figure 1F). We also confirmed that *Wt1* was significantly
109 downregulated in *Wt1*$^{+/-}$ ventricles in both transmural compartments (Figure 1F). Remarkably,
110 we detected increased *Scn5a* specifically in the (sub)epicardial side of *Wt1*$^{+/-}$ ventricles when
111 compared to controls (Figure 1E). This indicates that the increase in *Scn5a* expression detected
112 in cardiomyocytes of the RV/RVOT of *Wt1*$^{+/-}$ mice is driven by a mechanism primarily present in
113 the (sub)epicardial side of the ventricle, thus suggesting that epicardial *Wt1* inhibits *Scn5a*.

114 ECG analysis of adult (3-4 months) mice did not show any differences in PR-, QRS- and
115 QT duration in *Wt1*$^{+/-}$ mice compared to age-matched controls (Supplemental Figure 1A),
116 indicating no overt differences in cardiac electrophysiological properties *in vivo*. RV and RVOT
117 (sub)epicardial conduction was measured in more detail in Langendorff-perfused hearts of adult
118 mice using optical mapping (Supplemental Figure 1B, C). Overall, no differences in conduction
119 velocity (CV) were observed between *Wt1*$^{+/-}$ and control mice in either the RV or the RVOT. To
120 study the effect of *Wt1* haploinsufficiency on cellular electrical properties we measured action
121 potentials (AP) and sodium current (I_{Na}) in transmurally cardiomyocytes isolated from the entire
122 RV wall of adult control and *Wt1*$^{+/-}$ mice. AP upstroke velocity (V_{max}) was similar in
123 cardiomyocytes of both groups (Supplemental Figure 2A, B, Supplemental Table 1). In line with
124 this, no differences were observed in I_{Na} density or voltage dependence of (in)activation
125 (Supplemental Figure 2C-E, Supplemental Table 2). Resting membrane potential (RMP), AP
126 amplitude (APA) and AP repolarization parameters APD_{20}, APD_{50} and APD_{90} were also not
127 significantly different between RV cardiomyocytes from adult control and *Wt1*$^{+/-}$ mice
128 (Supplemental Figure 2A, B, Supplemental Table 2). Together, our data indicate that diminished
129 *Wt1* expression results in gene expression changes which are not sufficient to lead to an
130 electrophysiological phenotype.

131

132 **Diminished *Wt1* improves conduction in a severely challenged setting**

133 Next, we evaluated the possibility that electrophysiological changes driven by diminished
134 *Wt1* may only become apparent in the context of (severe) reduced conduction. To investigate
135 this, we crossed *Wt1*$^{+/-}$ mice with *Scn5a* haploinsufficient mice (*Scn5a*$^{+/-}$) to generate double
136 haploinsufficient mice (*Scn5a*$^{+/-}$;*Wt1*$^{+/-}$) and examined whether aging provides a sufficiently
137 sensitized setting. We therefore aged control, *Scn5a*$^{+/-}$ and *Scn5a*$^{+/-}$;*Wt1*$^{+/-}$ mice to ~15 months.
138 *In vivo* ECGs of adult mice (Supplemental Figure 3A) revealed that *Scn5a* haploinsufficiency led
139 to prolonged PR interval (Supplemental Figure 3B), while QRS duration was unchanged,
140 regardless of *Wt1* loss (Supplemental Figure 3C). Aging, independent of genotype, did not have
141 an effect on PR duration but did result in QRS interval prolongation in both *Scn5a*$^{+/-}$ and
142 *Scn5a*$^{+/-}$;*Wt1*$^{+/-}$, but not in control mice (Supplemental Figure 3). Indeed, an interaction effect
143 was borderline significant for QRS duration (p=0.0656), suggesting that aging may unmask a
144 more pronounced ventricular conduction phenotype in mice with only one copy of *Scn5a.* We
145 next investigated this in more detail by measuring epicardial CV in the RV and RVOT in aged
146 mice. We found slower CV in both longitudinal and transverse direction in *Scn5a*$^{+/-}$ and *Scn5a*$^{+/-}$
147 ;*Wt1*$^{+/-}$ RVs than in controls (Figure 2A). In the RVOT we observed slower conduction in
148 *Scn5a*$^{+/-}$ compared to controls, but this difference was not detected between *Scn5a*$^{+/-}$;*Wt1*$^{+/-}$ and
149 controls (Figure 2B). We then further challenged our experimental model (aged *Scn5a*$^{+/-}$ and
150 *Scn5a*$^{+/-}$;*Wt1*$^{+/-}$ animals) by suppressing I_{Na} availability through acute administration of the I_{Na}
151 blocker ajmaline. Since the relationship of CV and I_{Na} is not linear [34], CV differences are more
152 easily detected in the setting of reduced excitability. Optical mapping analysis in the presence of
153 ajmaline showed a significantly higher CV in the transverse direction of the RV and RVOT
154 (Figure 2C, D) of *Scn5a*$^{+/-}$;*Wt1*$^{+/-}$ compared to *Scn5a*$^{+/-}$ mice. Taken together, our data show that
155 decreased *Wt1* expression improves conduction in aged *Scn5a* haploinsufficient mice in the
156 setting of severely reduced conduction reserve.

157

158 ***WT1* is increased in pathologic conditions including BrS**

159 Because diminished *Wt1* was associated with increased *Scn5a* expression in
160 cardiomyocytes, as well as a less severe conduction slowing in *Scn5a* deficient mice, we
161 explored whether a correlation between *WT1* and *SCN5A* expression is present in human
162 cardiac samples. We conducted a regression analysis on previously published single-nuclei
163 RNAseq (snRNAseq) data of non-diseased human hearts [28]. Our analysis (pseudo-bulk) across
164 4 ventricular regions revealed a strong negative correlation between *WT1* and *SCN5A* (Figure
165 3A, Supplemental Table 3). This suggests that regions with higher *WT1* expression (i.e.
166 subepicardium) have tapered *SCN5A* levels and may therefore contribute to the transmural
167 expression gradient observed in mice (Figure 1E, F).

168 In normal hearts, *WT1* expression diminishes after birth, but it can become re-expressed
169 upon injury [23–26]. Recent snRNAseq studies have shown increased *WT1* in ventricular samples
170 of patients with congenital cardiac defects and hypertrophic cardiomyopathy (HCM) when
171 compared to non-diseased hearts [27–29]. Moreover, patients with arrhythmogenic
172 cardiomyopathy (ACM), a disease exhibiting overlapping pathology with BrS, showed increased
173 *WT1* when compared to healthy controls [35]. We then considered whether elevated *WT1*
174 expression occurs in the context of BrS. To test this, we obtained histological ventricular
175 sections from three *SCN5A* mutation-positive patients. Immunohistological staining for WT1
176 revealed distinct nuclear signal in 2 out of 3 of these hearts, while non-diseased hearts, neither
177 young (23 years) or old (79 years), showed barely any detectable staining (Figure 3B, C,
178 Supplemental Figure 5). These data indicate that increased *WT1*, and not its loss, is consistent
179 with the BrS phenotype. Moreover, patients with arrhythmogenic cardiomyopathy (ACM), a

180 disease exhibiting overlapping pathology with BrS, showed increased *WT1* when compared to
181 healthy controls [34].

182 Next, we considered whether *SCN5A* loss-of-function itself leads to induction of *WT1* at
183 any point in time. To address this, we performed lineage tracing experiments using *Wt1*^{Cre}
184 [18]*;R26R-mTmG* [36]*,* in which the Cre recombinase drives membrane GFP only in the *Wt1*
185 lineage, and studied this in the context of *Scn5a* haploinsufficiency. We quantified GFP+
186 cardiomyocytes of the RV, left ventricle (LV), and interventricular septum (IVS) of aged *Scn5a*$^{+/-}$
187 and control mice using cardiac troponin staining and flow cytometry. We found significantly
188 more GFP+ cardiomyocytes in the interventricular septum (IVS) and LV of *Scn5a*$^{+/-}$ mice when
189 compared to controls (Figure 4A). We next analyzed GFP+/cTnT+ cells on histological sections
190 and found increased double positive cells in mice with reduced *Scn5a* expression (Figure 4B,
191 C). These results indicate that life-long reduced *Scn5a*, as it occurs in patients with loss-of-
192 function *SCN5A* mutations, leads to induction of *Wt1* including in cardiomyocytes at any point
193 through life, which further solidifies the biological relevance of the inverse relationship between
194 *Wt1* and *Scn5a*.

195

196 **The BrS-associated noncoding variant region controls *Wt1* expression in the RV**

197 Given that diminished *Wt1* expression may confer a protective effect, and patients with
198 *SCN5A* loss-of-function mutations display elevated WT1, we proceeded to investigate how the
199 BrS-associated variant region (BAR) in chr11p13 impacts on *WT1.* We first identified candidate
200 regulatory elements within this region. Human epigenetic datasets, including ventricular-like
201 hiPS cardiomyocyte ATACseq (a measure of open chromatin regions) [37], CTCF ChIPseq [38], and
202 the EMERGE enhancer prediction track [39,40] reveal moderate epigenetic signatures overlapping
203 the BrS-associated variant region (Figure 5A). In the mouse orthologous region, ATACseq of

204 adult ventricular and neonatal sinus node tissue [41,42] shows open chromatin in the region
205 upstream of *Wt1*, with modest H3K27ac signatures [43] (Figure 5B). We therefore selected a 4903
206 bp region overlapping these epigenetic signatures for deletion using CRISPR/Cas9 (Figure 5C).
207 Homozygous deletion mice (*Wt1*$^{BAR/BAR}$) were born at the expected Mendelian ratios and
208 showed no overt morphological defects. Using RTqPCR, we determined the expression level of
209 *Wt1* in the (sub)epicardial and (sub)endocardial RVs and LVs of 6-week-old mice. *Wt1*$^{BAR/BAR}$
210 mice showed a ~45% increase in *Wt1* transcripts in the (sub)epicardial side of the RV, but not in
211 any other cardiac region assayed (Figure 5D). This observation indicates that the BAR contains
212 one or more regulatory elements that selectively represses expression of *Wt1* in the
213 (sub)epicardium of the RV, thus further supporting the notion that increased *WT1* contributes to
214 BrS pathophysiology.

215

216 **Overexpression of WT1 in hiPSC-derived cardiomyocytes leads to reduced sodium**
217 **current**

218 To determine the functional consequences of *WT1* overexpression in single
219 cardiomyocytes, we generated human induced pluripotent stem cell-derived cardiomyocytes
220 (hiPSC-CMs) by using an adapted protocol based on small molecule-mediated modulation of
221 the cWnt-pathway [44]. hiPSC-CMs were transfected using Lipofectamine 3000 with plasmids
222 containing either WT1-P2A-GFP or GFP only (which served as control) and measured peak
223 sodium (I_{Na}) in GFP-positive (GFP^+) hiPSC-CMs. Peak I_{Na} density was significantly lower in
224 hiPSC-CMs transfected with WT1 (Figure 6A, B); I_{Na} density at –20 mV was -87±10 and -54±7
225 pA/pF (p<0.05; t-test) in GFP^+ (n=16) and WT1 (n=12) overexpressing hiPSC-CMs. Neither the
226 voltage dependency of (in)activation nor the time constants of current inactivation, determined
227 at a test potential of -20 mV, were significantly different in hiPSC-cardiomyocytes with WT1

228 overexpression (Figure 6C, Supplemental Table 4), indicating that WT1 overexpression only
229 affects I_{Na} density and not the gating properties. While a previous study reported that loss
230 of *Wt1* in embryonic cardiomyocytes led to dysregulation of a potassium channel subunit which
231 is an important regulator of the transient outward (I_{to1}) current [22], we did not detect any
232 differences in I_{to1} density (Figure 6D, E) or I_{to1} gating properties (Figure 6F, Supplemental Table
233 4). AP measurements performed using dynamic clamp [45] demonstrated a significant decrease
234 in V_{max} in hiPSC-CMs overexpressing WT1 compared to controls (Figure 6G, H), in line with the
235 observed reduced I_{Na}. The RMP, APA, and AP repolarization parameters remained unchanged
236 upon WT1 overexpression (Figure 6H, Supplemental Table 4). Taken together, these
237 observations align with the effect of *Wt1* reduction on ventricular conduction demonstrated
238 herein, and suggest a modulatory contribution predominantly on depolarization.

239

240
241 **Discussion**

242 Here, we explored the role of *WT1*, a gene at a locus implicated in BrS by GWAS. Our
243 study reveals that diminished *Wt1* expression in mice leads to altered ion channel and cardiac
244 contraction gene expression, including a modest increase in *Scn5a* specifically in the
245 (sub)epicardial ventricular wall. We further provide evidence supporting an inverse relationship
246 between *WT1* and *SCN5A* expression in humans and identified increased *WT1* in pathological
247 conditions, including in *SCN5A* mutation positive patients. The interaction between these two
248 genes was further explored in a challenged setting provided by *Scn5a* haploinsufficiency. While
249 no differences in electrophysiological properties either *in vivo*, *ex vivo*, or in single
250 cardiomyocytes were detected under baseline conditions, diminished *Wt1* did improve
251 conduction under conditions of suppressed conduction reserve in the setting of advanced age
252 and acute ajmaline exposure. By deleting the BrS-associated noncoding region orthologue in
253 mice, we show that *Wt1* is a target of the REs likely affected by the disease-associated common
254 variants. Lastly, we demonstrate that overexpression of WT1 in hiPSC-derived cardiomyocytes
255 reduces I_{Na} density, thereby establishing *WT1* as a new player in the pathology of BrS.

256 A recent GWAS proposed *WT1* as the most likely candidate gene implicated in BrS in
257 chromosome 11, as indicated by the association signal in this locus [10]. In our study, we
258 demonstrate that lifelong reduction of *Wt1* leads to an upregulation of *Scn5a* predominantly on
259 the (sub) epicardial side of the cardiac ventricles. This finding points to a potential mechanism
260 by which *WT1* contributes to BrS through regulation of *SCN5A*, while also suggesting that
261 increased-, rather than decreased WT1 expression, is associated with the BrS pathological
262 state. Moreover, this highlights *WT1* as a potential key regulator in maintaining the transmural
263 ion channel gradient, which is essential for proper cardiac function. Correspondilngly, we
264 demonstrate that transient overexpression of WT1 in hiPSC-derived cardiomyocytes results in a

265 significant reduction in I_{Na}. This is consistent with existing knowledge regarding the loss of
266 $Na_V1.5$ function in the pathophysiology of BrS.

267 From an *in vivo* physiological perspective, discerning the impact of reduced *Wt1* proved
268 challenging. In order to observe an electrophysiological phenotype, it was necessary to
269 challenge WT1 haploinsufficient mice by aging and reducing sodium channel expression and
270 activity through acute exposure to ajmaline. This could be due to the complexity associated with
271 accurately measuring increased $Na_V1.5$ function in a laboratory setting. *Scn5a*$^{+/-}$ mice showed
272 increased QRS duration only with ageing, and not at young adult age as was shown before [46].[45].
273 A possible explanation for the mitigated phenotype is differences in used mouse strain, affecting
274 electrophysiological parameters [47,48].[46,47]. In this context, a rescue effect provided by *Wt1*
275 reduction (and consequently, increased *Scn5a*) can only be uncovered by further aggravating
276 the conduction phenotype. Together, these observations provide strong evidence for a role for
277 *WT1* in BrS pathophysiology through its impact on *SCN5A* expression.

278 The BrS-associated common variants in chromosome 11 are located in the noncoding
279 region upstream of *WT1*, and are therefore thought to impact on gene expression via REs [12–14].
280 RE activity is largely limited to the topologically-associating domain they share with their target
281 genes [49–51].RE activity is largely limited to the topologically-associating domain they share with
282 their target genes [48–50]. We presume that BrS risk variants disrupt the function of REs that
283 control *WT1* expression. Consequently, by deleting the mouse orthologue of the candidate RE,
284 we aim to model the genetic mechanism(s) at play in BrS patients. Indeed, we demonstrated
285 that loss of the BrS-associated variant-rich RE led to increased *Wt1* specifically in the
286 (sub)epicardial side of the RV *in vivo*. This finding further supports the notion that common
287 variants associated with increased BrS risk at this locus likely result in *WT1* upregulation, which
288 results in loss of $Na_V1.5$ function, thereby contributing to increased BrS risk. However, further

289 research is required to elucidate the transcriptional regulatory mechanisms driving the function
290 of this and other potential REs within the locus.

291 We speculate that decreased or increased *WT1* impacts on *SCN5A* expression in the
292 opposite direction via a paracrine or cell-autonomous mechanism. Although WT1 is known to
293 function as either a transcriptional activator or repressor depending on its binding partners
294 (reviewed in [52]), not all evidence supports a cell-autonomous mechanism. We show that *Wt1*
295 expression was below detection in the cardiomyocyte-enriched fraction, yet *Scn5a* was
296 upregulated in *Wt1*$^{+/-}$ cardiomyocytes. This result may indicate that deregulation of *WT1* in non-
297 cardiomyocytes, via a paracrine process, affects gene expression in cardiomyocytes. The
298 specific cell-type in question has yet to be identified. Alternatively, *WT1* may be expressed at
299 low levels, in a small proportion, or only transiently in cardiomyocytes, making it difficult to
300 detect any decrease in expression, and thereby introducing further challenges for the
301 interpretation of data. Our study, along with others [27–29,35], indicates that elevated *WT1*
302 expression is linked to pathological states. Therefore, only in the context of increased WT1 we
303 may be able to uncover a cell-autonomous transcriptional effect on *SCN5A*.

304 It is also a possibility that WT1 affects *SCN5A* via a non-transcriptional mechanism.
305 Recent studies have revealed that WT1 can also control gene expression by modulating the
306 epigenetic landscape via interacting with TET family proteins [53,54]. WT1 is also known to
307 modulate topological switch mechanisms involving global changes in chromatin access to
308 provide context for specific gene activation or repression. For example, it acts as a
309 transcriptional activator of *Wnt4* in the developing kidney mesenchyme undergoing
310 mesenchymal-to-epithelial transformation, and a repressor of *Wnt4* in epicardial cells poised for
311 EMT [55]. WT1 may also function post-transcriptionally according to a study which showed that
312 one of the WT1 isoforms localizes and interacts with splicing factors in kidney cells [56].
313 Furthermore, WT1 has been shown to regulate mitotic checkpoint via direct interaction with the

314 spindle assembly checkpoint protein MADS2 [57]. Thus, additional research is needed to rule out
315 the possibility of a non-transcriptional contributing mechanism.

316 Conversely, decreased *SCN5A/Scn5a* expression also results in induction of *WT1/Wt1*,
317 as demonstrated by *Wt1*-lineage tracing on *Scn5a*$^{+/-}$ mice and histological staining of patient
318 hearts with an *SCN5A* mutation. This suggests a tightly regulated interplay and the dynamic
319 balance influences cellular processes including cardiac conduction. Once either of these genes
320 shifts towards a pathologic state (i.e. increased *WT1* or decreased *SCN5A*), it may trigger a
321 potential maladaptive cyclic mechanism which progressively exacerbates organ dysfunction.

322 In conclusion, our data establish a role for the transcription factor *WT1* in the
323 pathophysiology of BrS, at least in part, through modulating expression and function of the
324 cardiac sodium channel *SCN5A*. Additionally, we present an explanation for the association of
325 the noncoding region in chromosome 11 with BrS in patients. Beyond rare coding loss-of-
326 function variants in *SCN5A*, we expect that the aggregate effect of common variants at one or
327 more disease-associated loci impact on $Na_V1.5$ function and thereby BrS susceptibility.

328

329
330 **Methods**

331 Ethics statement

332 Housing, husbandry, all animal care and experimental protocols were in accordance with
333 guidelines from the Directive 2010/63/EU of the European Parliament, and Dutch government.
334 Protocols were approved by the Animal Experimental Committee of the Amsterdam University
335 Medical Centers. Animal group sizes were determined based on previous experience.

336

337 Mice

338 *Scn5a*$^{+/-}$ and *Wt1*^{Cre} mice were generated as described previously [18,46], respectively.
339 129S4/SvJae *Wt1*$^{GFPCre/+}$ and *R26-mTmG* mice were obtained from Jackson Laboratories (stock
340 numbers 010911, 007676, respectively). Given that the GFP-Cre insertion in the *Wt1* allele
341 replaces exon 1 and thereby produces a null allele [58], the mice are herein referred to as *Wt1*$^{+/-}$.
342 *Wt1*$^{+/-}$ mice were crossed with *Scn5a*$^{+/-}$ to generate *Scn5a*$^{+/-}$;*Wt1*$^{+/-}$. *Wt1*^{Cre} mice were crossed
343 first to *R26-mTmG* followed by *Scn5a*$^{+/-}$ for lineage tracing experiments.

344 *Wt1*$^{BAR/BAR}$ mice were generated using CRISPR/Cas9. Guide RNA (sgRNA) target sites were
345 designed with PrimerQuest™ program (IDT, Coralville, Iowa, USA. Accessed 12 December,
346 2018. https://www.idtdna.com/SciTools). The Alt-R® CRISPR-Cas9 crRNA, Alt-R® CRISPR-
347 Cas9 tracrRNA (IDT #1072532) and Alt-R® S.p. Cas9 Nuclease V3 (IDT #1081058) were
348 ordered at IDT. One-cell FVB/NRj zygotes were microinjected via the "Mouse zygote
349 microinjection Alt-R™ CRISPR-Cas9 System ribonucleoprotein delivery protocol" with 20 ng/µl
350 Cas9 Nuclease and 10 ng/µl guide RNA to generate mouse founders. The guide sequences
351 were as follows: 1) GGATTTAGGTCAAGATTCAC, 2) CACCACCATGGGATTCCTAA.
352 Deletions were validated by PCR using the following primers: Forward 1)

353 CTCTGGCTGCTGAAGGGATT, Reverse 1) CTAGCTCTTACTGGCCACCG, Reverse 2)
354 GAGAACAGAGCCCAGGAAGG and Sanger sequencing. The deleted region spans
355 chr2:105107107-105112009. To obtain stable lines, the founders were backcrossed with wild-
356 type FVB/NJ mice and maintained on FVB/NJ background ordered from the Jackson laboratory
357 (#100800). For tissue harvest, animals were euthanized by 20% CO_2 inhalation followed by
358 cervical dislocation.

359

360 Isolation of CM nuclei

361 Nuclei isolation was performed as previously described [59] with the following changes: snap
362 frozen adult left and right atria from adult male and female mice were trimmed and
363 homogenized in lysis buffer containing RNase inhibitor using an Ultra-Turrax homogenizer.
364 Samples were further homogenized with a loose pestle douncer (10 strokes). After a 10-min
365 incubation in the lysis buffer, an additional 10 strokes were performed with a tight pestle. The
366 lysis procedure was monitored by light microscopy to ensure complete tissue and cell lysis and
367 efficient nuclear extraction. The crude lysate was successively passed through 100 and 30µm
368 mesh filters. The final lysate was spun at 1000 × g for 5 min and the resulting pellet was
369 resuspended in 500 µl staining buffer (5% BSA in PBS) supplemented with RNAse inhibitor.
370 Isolated nuclei were incubated with rabbit polyclonal antibodies specific for pericentriolar
371 material 1 (PCM1) (Sigma-Aldrich; HPA023370) at a dilution of 1:400 for 1 h rotating at 4 °C.
372 Next, Alexa Fluor 647-conjugated donkey-anti-rabbit 647 antibodies (ThermoFisher Scientific A-
373 31573; 1:500 dilution), and DAPI (1:1000 dilution) were added and the incubation was continued
374 for an additional hour. Samples were spun at 1000 × g for 10 min and washed with 500 µl
375 staining buffer before resuspension in 500 µl staining buffer supplemented with RNAse inhibitor.
376 Intact CM nuclei were sorted on a BD Influx FACS on the basis of DAPI and Alexa Fluor 647

377 positivity into cold BL+TG buffer from the ReliaPrep RNA Tissue Miniprep System (Promega,
378 Z6112) for RNA isolation. RNA was isolated following a gDNA depletion step according to the
379 manufacturer's instructions.

380

381 RNAseq

382 For RNA isolated from cardiac nuclei, 500 pg was used for library generation with the Ovation
383 RNA-seq v2 kit (NuGEN M01206) kit. Libraries were prepared with the UltraLow V2 (NuGen) kit
384 and sequenced on the HiSeq4000 system (Illumina) with 50 bp single-end reads. 4 control and
385 4 $Wt1^{+/-}$ samples were sequenced. Reads were mapped to the mm10 build of the mouse
386 transcriptome using STAR [60]. Differential expression analysis was performed using the DESeq2
387 package based on a negative binomial distribution model. P-values were corrected for multiple
388 testing using the false discovery rate (FDR) method of Benjamini-Hochberg. We have used 0.05
389 as FDR control level. PANTHER32 was used for gene ontology (GO) biological process
390 analysis. Benjamini–Hochberg correction was performed for multiple testing-controlled P values.
391 Statistically significant enriched terms were functionally grouped and visualized.

392

393 RTqPCR

394 Total RNA was isolated from (sub) epicardial and (sub) endocardial ventricular sides of 12-16-
395 (*Wt1+/-*) or 6-week-old (*Wt1BAR/BAR*) male and female mice using ReliaPrep RNA Tissue
396 Miniprep System (Promega, Z6112) according to the manufacturer's protocol. cDNA was
397 reverse transcribed with oligo dT primers from 500ng of total RNA, according to the
398 manufacturer's protocol of the Superscript II Reverse Transcriptase system (Thermo Fisher
399 Scientific, 18064014). Expression levels of candidate target genes were determined by

400 quantitative real-time PCR using a LightCycler 480 Instrument II (Roche Life Science,
401 05015243001). Expression levels were measured using LightCycler 480 SYBR Green I Master
402 (Roche, 04887352001) and the primers had a concentration of 10 pmol/L. The amplification
403 protocol consisted of 5 minutes 95 °C followed by 45 cycles of 10 seconds 95°C, 20 seconds
404 60°C and 20 seconds 72°C. Relative start concentration (N0) was calculated using LinRegPCR
405 [61]. Values were normalized to one or two reference genes per experiment (Hprt and Ppia). The
406 primer sequences are as follows: (all 3' to 5') Hprt: TGTTGGATATGCCCTTGACT,
407 GATTCAACTTGCGCTCATCT; Ppia: GGGTGGTGACTTTACACGCC,
408 CTTGCCATCCAGCCATTCAG; Scn5a: GGGACTCATTGCCTACATGA,
409 GCACTGGGAGGTTATCACTG; Wt1: TTCAAGGACTGCGAGAGAAGG,
410 TATGAGTCCTGGTGTGGGTCT.

411

412 *In vivo* electrocardiogram

413 12-16 (adult) or 65-67 week old male mice were anesthetized with 5% Isoflurane
414 (Pharmachemie B.V. 061756) and placed on thermostated mat (36°C) with a steady flow of
415 1.5% isoflurane during all experiments. Electrodes were inserted subcutaneously in the limbs
416 and connected to an ECG amplifier (Powerlab 26T, AD Instruments). The electrocardiogram
417 (ECG) was measured for 5 minutes. ECG parameters were determined in Lead I based on 30
418 seconds of the recording. Only male mice were used given that BrS is more prevalent in males.

419

420 Optical mapping and ajmaline exposure

421 Following ECG measurement, mice were sacrificed by cervical dislocation. The hearts were
422 excised, cannulated and mounted on a Langendorff perfusion setup. Hearts were submerged in,

423 and retrogradely perfused with 37 °C Tyrode's solution containing (in mmol/L): NaCl 128, KCl
424 4.7, $CaCl_2$ 1.45, $MgCl_2$ 0.6, $NaHCO_3$ 27, NaH_2PO_4 0.4 and glucose 11 (pH maintained at 7.4 by
425 equilibration with a mixture of 95% O_2 and 5% CO_2). The excitation-contraction uncoupler
426 blebbistatin (10 µmol/L, Bio-Techne Ltd) was added in order to prevent movement artifacts.
427 During the optical mapping experiments, pseudo-electrograms were recorded by placing three
428 electrodes at ~0.5 cm distance of the heart in the Einthoven configuration. After ~10 minutes
429 recovery period, hearts received a 0.4 ml bolus of 20 µmol/L Di-4 ANEPPS (Molecular Probes),
430 the dye used for visualizing optical action potentials. Only hearts showing a regular sinus rhythm
431 that was stabilized within the first two minutes were included for analyses. Conduction velocities
432 were measured while pacing at the RV and the RVOT at a cycle length of 120 ms at twice the
433 stimulation threshold. Hereafter, hearts were treated continuously with ajmaline (1.5 µmol/L,
434 Carinopharm) and after a 10 minutes incubation period, the protocol was repeated. The average
435 length of the full protocol was 66.7± 1.1 minutes. Optical signals were analyzed with previously
436 published software [62], using Matlab2018. In short, optical signals were spatially (7x7 bin) and
437 temporally (0-150 Hz) filtered and local activation was defined as the maximum positive dV/dt of
438 the depolarization phase of the action potential. Conduction velocity was analyzed in two
439 transversal- (RV and RVOT) and two longitudinal (RV) directions and averaged for each
440 direction.

441

442 Generation, dissociation and transfection of hiPSC-CMs

443 The hiPSCs (LUMC0099iCTRL04 line) were maintained on growth factor reduced matrigel
444 (Corning, USA) -coated plates in mTeSR1 (Stem Cell Technologies, Canada) medium at 37°C
445 (with 5% CO_2 and 20% O_2) and passaged every 3-4 days.

446 Cardiomyocytes were derived by using an adaptation of a published method [44]. Briefly, upon
447 reaching 85-95% confluence differentiation of the hiPSCs started by switching the medium to
448 RPMI 1640 (ThermoFisher Scientific, USA) supplemented with B27 minus insulin
449 (ThermoFisher Scientific, USA) and 213ug/ml L-Ascorbic Acid 2-phosphate (hereunder referred
450 to as -I+AA medium) and containing 6 μM CHIR99021 (Selleckchem, USA) for 72 hours. The
451 medium was than replaced with -I+AA medium containing 2 μM Wnt-C59 (MedChemExpress,
452 USA) for Wnt signaling inhibition and kept for other 72 hours on the cells. From day 8 onward,
453 hiPSC-CMs were cultured in RPMI 1640 supplemented with B27 plus insulin (ThermoFisher
454 Scientific, USA), without ascorbic acid and refreshed every 3-4 days until day 30.

455 For transfection and subsequent single-cell electrophysiological analysis, hiPSC-CMs cultures
456 were dissociated with 1× TrypLE Select Enzyme (ThermoFisher Scientific, USA) for 10 minutes
457 at 37ºC, collected, centrifuged and reseeded at a density of approximately $4x10^3$ cells per
458 coverslip in presence of RPMI 1640 supplemented with B27 plus insulin and L-Ascorbic Acid 2-
459 phosphate (+I+AA medium). The glass coverslips were precoated with GFR matrigel/gelatin at
460 50/50 ratio.

461 Transfection was performed using Lipofectamine 3000 reagent (ThermoFisher) according to
462 manufacturer's protocol. Two pcDNA3.1 plasmids with CMV promotor and a P2A-eGFP site,
463 containing one of two common *WT1* isoforms were used together in 1:1 ratio: isoform D
464 (NM_024426.4, OHu27351, Genscript) and isoform B (NM_024424.3, OHu27419, Genscript).
465 For the control, the same plasmid without *WT1* was used ("GFP-only"). Amount of plasmid (in
466 ng) was chosen based on plasmid size (WT1-GFP 7.7kb, GFP 6.1kb), to ensure equal plasmid
467 copies per condition. For each well in a 24-well plate, 0.75μl (for WT1) or 0.59μL (for GFP-only)
468 lipofectamine was dissolved in 25μl RPMI (without glucose) and 500ng WT1 or 396 ng GFP-
469 only plasmid with 1μl (for WT1) or 0.79μl (for GFP) P3000 in 25μl RPMI, after which these two
470 were gently mixed (i.e. lipofectamine μl to DNA μg ratio 1.5) and incubated 10-15 minutes.

471 Mixes were added to the cells and removed and replaced by culture medium after 3 days, and
472 patched the next day.

473

474 RV cardiomyocyte isolation

475 Freshly excised hearts of male mice were cannulated and mounted on a Langendorff setup,
476 retrogradely perfusing oxygenated modified Tyrode's solution at 37 °C containing (in mmol/L):
477 NaCl 140, KCl 5.4, $CaCl_2$ 1.8, $MgCl_2$ 1.0, glucose 5.5, and HEPES 5.0; pH 7.4 (adjusted using
478 NaOH). After 10 minutes, hearts were perfused with nominally calcium-free solution containing
479 (in mmol/L): $CaCl_2$ 0.01, creatine 10.7. After a consecutive 10 minutes, hearts were digested by
480 addition of Liberase TM (0.032 mg/mL, Roche) and elastase (1.6 U/mL, SERVA Electrophoresis
481 GmbH), while perfusing for ~15 minutes. Hearts were washed in calcium-free solution
482 containing 1% bovine serum albumin fraction V, fatty acid free (Roche). The RV was removed
483 and cut into small pieces after further dissociating by pipette trituration to obtain single
484 cardiomyocytes, which were washed in perfusion solution while up-titrating $CaCl_2$ to 1.8 mmol/L.
485 Isolated RV cardiomyocytes were stored at room temperature in modified Tyrode's solution and
486 used for AP and I_{Na} recordings within 2-3 hours.

487

488 Cellular electrophysiology

489 *Data acquisition and analysis:* APs and I_{to1} were recorded with the amphotericin-B perforated
490 patch-clamp technique while I_{Na} was recorded with ruptured patch-clamp technique, using an
491 Axopatch 200B patch-clamp amplifier (Molecular Devices, San Jose, CA, USA). Voltage control,
492 data acquisition, and analysis were done using custom software [63] and pClamp10.6/Clampfit
493 (Molecular Devices, San Jose, CA, USA). Borosilicate glass patch pipettes (GC100F-10;

494 Harvard Apparatus, Waterbeach, UK) with a tip resistance of 2-2.5 MΩ were used. Signals were
495 low-pass-filtered with a cutoff of 5 kHz and digitized at 20 kHz for I_{Na}, 30 kHz for I_{to1}, and 40 kHz
496 for APs. Cell membrane capacitance was calculated by dividing the time constant of the decay
497 of the capacitive transient after a −5 mV voltage step from −40 mV by the series resistance [45].
498 Series resistance was compensated for >80%. I_{to1} and APs were corrected for the calculated
499 liquid junction potential. Following the procedure of Veerman et al. [64], we selected single,
500 spontaneously beating, GFP^+ or WT1 overexpressing hiPSC-CMS showing regular,
501 synchronous contractions in modified Tyrode's solution, after which this extracellular solution
502 was switched to a solution suitable for specific measurements as indicated below. For mouse,
503 recordings were made from quiescent cardiomyocytes.

504

505 *Action potential measurement:* APs were measured in hiPSC-cardiomyocytes and mouse
506 cardiomyocytes at 37°C in modified Tyrode's solution, containing (in mmol/L): NaCl 140, KCl
507 5.4, $CaCl_2$ 1.8, $MgCl_2$ 1.0, glucose 5.5, HEPES 5.0; pH 7.4 (NaOH). Patch pipettes were filled
508 with a solution containing (in mmol/L): K-gluconate 125, KCl 20, NaCl 5 (hiPSC-CMs) or 10
509 (mouse), amphotericin-B 0.44, HEPES 10; pH of 7.2 (KOH). APs were elicited at 4 Hz in mouse
510 CMs and at 1 Hz in hiPSC-CMs by 3 ms, 1.2-1.4 x threshold current pulses through the patch
511 pipette. To overcome the lack of the inward rectifying potassium current (I_{K1}) in hiPSC-
512 cardiomyocytes, which limits the functional availability of I_{Na} and I_{to} [65], we injected an 2 pA/pF in
513 silico I_{K1} with kinetics of Kir2.1 channels through dynamic clamp, as previously described and
514 validated [66]. AP parameters were analyzed from 10 consecutive APs and averaged.

515

516 *Sodium current measurement:* I_{Na} was measured at room temperature (~20°C). The bath
517 solution for I_{Na} recordings in mouse CMs contained (in mmol/L): NaCl 7.0, CsCl 133, $CaCl_2$ 1.8,

518 $MgCl_2$ 1.2, glucose 11.0, nifedipine 0.005, HEPES 5.0; pH 7.4 (adjusted with CsOH), while
519 hiPSC-CMs were perfused with an external solution containing (in mmol/L): NaCl 20, CsCl 120,
520 $CaCl_2$ 1.8, $MgCl_2$ 1.0, glucose 5.5, nifedipine 0.010, HEPES 5.0; pH 7.4 (adjusted with CsOH).
521 Pipette solution was composed of (mmol/L): NaCl 3.0, CsCl 133, $MgCl_2$ 2.0, Na_2ATP 2.0, TEACl
522 2.0, EGTA 10, HEPES 5.0; pH 7.2 (adjusted with CsOH). I_{Na} was recorded with a double-pulse
523 protocol from a holding potential of –120 mV (see inset of Supplemental Figure 2C and Figure
524 6A; cycle length of 5 seconds). During the first 500 ms depolarizing pulses, I_{Na} activates and the
525 currents analyzed here are used to determine I-V relationships and the voltage dependency of
526 activation. For the latter, the I-V relationships were corrected for driving force and normalized to
527 maximal current. The second pulse is used to determine the voltage dependency of inactivation
528 and currents were normalized to the largest I_{Na}. I_{Na} was defined as the difference between peak
529 and steady-state current and densities were calculated by dividing current amplitude by C_m.
530 Voltage dependency curves of activation and inactivation were fitted with Boltzmann function:
531 $I/I_{max}=A/\{1.0+\exp[(V_{1/2}-V)/k]\}$, where $V_{1/2}$ is the half-maximal voltage of (in)activation, and k is the
532 slope factor (in mV). The time course of current inactivation was fitted by a double-exponential
533 equation: $I/I_{max}=A_f \times \exp(-t/\tau_f)+A_s \times \exp(-t/\tau_s)$, where A_f and A_s are the fractions of the fast and slow
534 inactivation components, and τ_f and τ_s are the time constants of the fast and slow inactivating
535 components, respectively.

536

537 *Transient outward K^+ current measurements.* I_{to1} was measured under conditions similar as
538 mentioned for APs, but 0.25 mmol/L $CdCl_2$ was added to the modified Tyrode's to blocks $I_{Ca,L}$ [67]
539 [67] which also strongly inhibits I_{Na} [68]. Suppression of these inward currents allows a more
540 accurate determination of I_{to1}. I_{to1} was measured using a double pulse protocol from a holding
541 potential of -80 mV (see inset Figure 6D; cycle length of 5 seconds). The first pulse was used to
542 determine the I-V relationship; the second pulse was used to analyze the voltage dependency of

543 inactivation. I_{to1} was defined as the difference between peak and steady state current and
544 densities were calculated by dividing current amplitude by C_m. Voltage dependence of
545 inactivation curves was fitted with the above-mentioned Boltzmann function and time course of
546 current inactivation was fitted by a mono-exponential equation: $I/I_{max}=A_f \times \exp(-t/\tau_f)$.

547

548 Analysis of human snRNAseq data

549 To assess the relationship between *SCN5A* and *WT1* expression in human heart tissue, we
550 leveraged the Reichart et al. dataset. Reichart et al. performed snRNAseq on 61 explanted end-
551 stage cardiomyopathy hearts, as well as 18 hearts from non-failing donors. The authors
552 performed snRNAseq across various ventricular regions, including the left ventricle, the right
553 ventricle, the interventricular septum, and the apex. For our analyses, we restricted to the 18
554 non-failing hearts and removed nuclei with 'unknown' annotations, leaving a total of 266,219
555 high-quality nuclei. For the regression analyses, we performed pseudo-bulking on the count
556 matrix, where counts for each gene were collapsed per donor/region combination. Lowly-
557 expressed genes were removed using the function *filterByExpr()* from the *edgeR* package
558 (using design: ~0 + region + sex + development_stage), after which *SCN5A* and *WT1* remained
559 in the dataset. Count data were normalized using the *DESeq2* package, using functions
560 *DESeqDataSetFromMatrix()*, *estimateSizeFactors()*, and finally *counts()* with flag
561 'normalized=TRUE'. To regress the normalized expression of *WT1* on the normalized
562 expression of *SCN5A*, we utilized a mixed negative binomial regression model, implemented in
563 R-package *glmmTMB*, with the formula: *WT1* ~ *SCN5A* + sex + development_stage + region +
564 (1 | donor).

565

566 Histology

567 Human RV, LV and interventricular septum 7 μm histological sections were obtained from the
568 department of pathology at Amsterdam UMC. Sections were stained with a WT1-antibody
569 (Abcam/Epitomics AC9115, clone EP122) diluted 1:50 using HIER (heat-induced epitope
570 retrieval) (Tris-EDTA, pH 9.0) at 100°C. Sections were examined with a Leica imaged on a
571 DSM5000 widefield microscope.

572 Adult mouse hearts were fixed overnight in 4% paraformaldehyde in PBS, dehydrated in a
573 ascending ethanol series, paraffin embedded and sectioned at 8 *μ*m. Sections were
574 deparaffinized with xylene, rehydrated in descending ethanol series and treated with HIER
575 (citrate-based antigen unmasking solution, Vector, H-3300-250) at 100°C. After permeabilization
576 (Triton-X 0.5%) and blocking (BSA 5%), sections were stained with anti-cTnT (1:400, HyTest
577 Ltd 4T19/2), anti-GFP (1:300, Abcam Cat ab13970), anti-WGA-555 (1:200, ThermoFisher
578 W32464) and DAPI. Stained sections were imaged and photographed with a Leica DM6
579 microscope.

580

581 Flow cytometry

582 Cell isolations for flow cytometry experiments were carried out according to a previously
583 published protocol [69]. In short, after extracting the heart, the ascending aorta was clamped and
584 a collagenase buffer was injected into the apex of the left ventricle. Then the atria were removed
585 and the right ventricular free wall, left ventricular free wall and septum were separately
586 dissociated by trituration. After suspending cells in stop solution (containing FBS), they were
587 passed a 100μm strainer, centrifuged at low speed and stained for the cardiac marker cTnT. For
588 the latter, cells were incubated 15 minutes in permeabilizing-blocking buffer (PBS with 0.1%
589 saponin and 5% FBS), incubated with anti-cTnT (HyTest Ltd Cat 4T19/2, 1:400) for 1 hour and
590 with secondary antibody (AF647 donkey anti-goat IgG H+L, Life A21447, 1:200) for 15 minutes,

591 all at room temperature. Cells were confirmed to be all cardiomyocytes using a negative control
592 without primary antibody. For compensation control, littermates without Cre were used. Cells
593 were dissolved in FACS buffer (PBS with 0.5% BSA and 2mM EDTA) and measured with a
594 LSRFortessa Flow Cytometer (BD Biosciences). FlowJo was used for analysis. Forward and
595 side scatter information was used for gating of non-debris single cells and from these cells, the
596 amount of endogenous tdT positive and GFP positive cells was quantified. For each experiment
597 *Scn5a*$^{+/+}$ and *Scn5a*$^{+/-}$ hearts were used in parallel, with researchers being blinded for the
598 genotype during experiment and analysis.

599

600 Statistics

601 The experimenters were blind to genotypes during all measurements and outcome assessment.
602 Datasets were tested for normality using Shapiro-Wilk test unless specified otherwise. Whole
603 isolated tissue RT-qPCR were analyzed with ANOVA with Welch's correction followed by
604 unpaired t-tests with Welch's correction (Figure 1), or 2-way ANOVA followed by Šídák's
605 multiple comparisons test and adjusted p-values are shown (Figure 5). *In vivo* electrophysiology
606 and optical mapping measurements were analyzed with unpaired t tests for 2 group
607 comparisons, and 2-way ANOVA followed by Tukey's multiple comparison test for aging
608 experiments comparing 3 groups. For single cell electrophysiology, data are expressed as
609 mean±SEM. Statistical analysis was carried out with SigmaStat 3.5 software (Systat Software,
610 Inc., San Jose, CA, USA). Normality and equal variance assumptions were tested with the
611 Kolmogorov–Smirnov and the Levene median test, respectively. Significance between
612 parameters of two groups was tested using unpaired Student's t-test, or in case of a failed
613 normality and/or equal variance test, by Mann-Whitney Rank Sum Test. Data of I-V
614 relationships was tested for significance using the two-way repeated measures ANOVA followed

615 by pairwise comparison using the Student–Newman–Keuls test. $P<0.05$ defines statistical
616 significance.

617 For the flow cytometry data, a general linear mixed model was used after rank transformation of
618 GFP percentages due to non-normally distributed residuals. Bonferroni post-hoc pairwise
619 comparisons of regions and Mann-whitney U pairwaise tests of genotypes were used.

620 Data are presented as individual data points and mean or mean ± standard error of the mean
621 (SEM) and $p<0.05$ defines statistical significance. Statistical analysis was performed using
622 GraphPad Prism 10 and SPSS.

623

624
625 **Figure Legends**

626 **Figure 1.** Diminished *Wt1* leads to increased *Scn5a*. A) Schematic depicts approach for
627 isolating cardiomyocyte (CM) nuclei of the RV and RVOT. B) Volcano plot shows differentially
628 expressed transcripts between control (n=4) and *Wt1*$^{+/-}$ (n=4) cardiomyocytes. Dark red and
629 light red dots indicate significantly upregulated genes by raw p-value and p-adjusted for multiple
630 testing, respectively. Correspondingly, dark blue and light blue dots indicate downregulated
631 genes. C) Gene ontology (GO) analysis of up-and downregulated genes in *Wt1*$^{+/-}$
632 cardiomyocytes. P-values were adjusted for multiple testing using the false discovery rate (FDR)
633 method of Benjamini-Hochberg. D) Heatmap depicting deregulated genes and their adjusted p-
634 values (all $p<0.05$) involved in electrical conduction. Scale denotes fold change. E, F) *Hprt*-
635 corrected expression of *Scn5a* (E) and *Wt1* (F) from adult control (n=6) and *Wt1*$^{+/-}$ (n=6)
636 ventricular (sub)endocardium and (sub)epicardium determined by RT-qPCR. Significant p-
637 values were determined with Welch's ANOVA followed by unpaired *t*-tests with Welch's
638 correction.

639

640 **Figure 2.** Reduced *Wt1* expression improves conduction in the setting of severely reduced
641 conduction in aged *Scn5a*$^{+/-}$ mouse hearts. A) Typical examples of RV longitudinal and
642 transversal- and B) RVOT conduction with respective average conduction velocity (CV) of aged
643 control (n= 10), *Scn5a*$^{+/-}$ (n= 9) and *Scn5a*$^{+/-}$;*Wt1*$^{+/-}$ (n= 9). RV, right ventricle; RVOT, right
644 ventricular outflow tract. C) Typical examples and average CV of RV longitudinal and
645 transversal direction, and D) RVOT in aged *Scn5a*$^{+/-}$ and *Scn5a*$^{+/-}$;*Wt1*$^{+/-}$ mice after acute
646 administration of ajmaline (n=7). Statistical significance was determined with ANOVA followed
647 by pairwise Tukey's multiple comparison tests for A and B, and unpaired *t*-tests for C and D.

648

649 **Figure 3.** A negative correlation between *WT1* and *SCN5A* expression. A) Partial regression
650 plot for mixed negative binomial model between *WT1* and *SCN5A* from 18 healthy donors
651 across 4 ventricle regions in pseudo-bulk. Axes represent the covariate-adjusted log-
652 transformed expression of *WT1* and *SCN5A.* Corresponding statistics are added, where r_s
653 represents the Spearman's correlation coefficient, while z and p represent the Z-value and P-
654 value from the mixed negative binomial regression respectively. For untransformed data see
655 Supplemental Figure 4. B, C) Representative images of non-diseased (B) *and SCN5A* mutation
656 carrier (C) RV histological sections stained for WT1. Brown arrowheads indicate WT1 signal.

657

658 **Figure 4.** Increased *Wt1*-lineage cells in *Scn5a* haploinsufficient hearts. A) Percent
659 GFP+/cTnT+ cells in LV, IVS, and RV in control (n= 5) and *Scn5a*$^{+/-}$ (n=6) mice as determined
660 by FACS. Significance determined by a general linear mixed model and post-hoc tests. B-D)
661 Representative images of histological sections of control and *Scn5a*$^{+/-}$ hearts. LV, left ventricle;
662 RV, right ventricle; IVS, interventricular septum.

663

664 **Figure 5.** Deletion of BrS-associated region in mouse orthologue leads to increased *Wt1*
665 selectively in (sub) epicardium of RV. A) UCSC browser view of the human BrS-associated
666 locus in chr11 including ATACseq from hiPS ventricular cardiomyocytes (black), EMERGE
667 (red), CTCF ChIPseq (red bars), and conservation track. B) Mouse orthologue of the human
668 region shown in panel B including ATACseq of ventricular cardiomyocytes and Hcn4+ sinoatrial
669 node (SAN) cells, H3K27ac ChIPseq from whole adult hearts, and EMERGE. C) Zoom-in of
670 panel B depicting the deleted region (BAR) in blue. D) Reference gene-corrected expression of
671 *Wt1* from isolated (sub) epicardial and (sub)endocardial sides of the RV and LV determined by
672 RTqPCR of *Wt1*$^{BAR/BAR}$ (n=9) and control littermates (n=9). Statistical significance was

673 determined with 2-way ANOVA followed by pairwise comparisons with Tukey's multiple
674 comparison tests. P values are shown.

675

676 **Figure 6.** WT1 overexpression in hiPSC-cardiomyocytes reduces sodium current (I_{Na}) and
677 action potential (AP) upstroke velocity. A) Voltage clamp protocol and representative traces of
678 I_{Na} activated during depolarizing steps from -120 to -20 mV. B) Average current-voltage (I-V)
679 relationships of I_{Na}. C) Average voltage dependence of (in)activation curves. Solid lines
680 represents the fitted Boltzmann function ($I/I_{max}=A/\{1.0+\exp[(V_{1/2} -V)/k]\}$). D) Voltage clamp
681 protocol and representative traces of the transient outward potassium current (I_{to1}) activated
682 during depolarizing steps from -80 to 60 mV. E) Average I-V relationships of I_{to1}. F) Average
683 voltage dependence of (in)activation curves. Solid lines represent the fitted Boltzmann function
684 for inactivation. G) Typical APs measured at 1 Hz. The inset shows the AP upstroke velocity
685 (V_{max}). **H.** Average AP parameters. RMP, resting membrane potential; APA, AP amplitude;
686 APD_{20} APD_{50}, and APD_{90}, AP duration at 20, 50 and 90% of repolarization, respectively; *
687 Indicates $P<0.05$ by Two-Way ANOVA or unpaired t-test.

688

References

1. Marsman, E. M. J., Postema, P. G. & Remme, C. A. Brugada syndrome: update and future perspectives. *Heart* **108**, 668–675 (2022).
2. Offerhaus, J. A., Bezzina, C. R. & Wilde, A. A. M. Epidemiology of inherited arrhythmias. *Nat. Rev. Cardiol.* **17**, 205–215 (2020).
3. Priori, S. G. *et al.* 2015 ESC Guidelines for the management of patients with ventricular arrhythmias and the prevention of sudden cardiac death: The Task Force for the Management of Patients with Ventricular Arrhythmias and the Prevention of Sudden Cardiac Death of the European Society of Cardiology (ESC)Endorsed by: Association for European Paediatric and Congenital Cardiology (AEPC). *Eur. Heart J.* **36**, 2793–2867 (2015).
4. Miles, C. *et al.* Subepicardial Cardiomyopathy: A Disease Underlying J-Wave Syndromes and Idiopathic Ventricular Fibrillation. *Circulation* **147**, 1622 (2023).
5. Boukens, B. J. *et al.* Reduced Sodium Channel Function Unmasks Residual Embryonic Slow Conduction in the Adult Right Ventricular Outflow Tract. *Circ. Res.* **113**, 137–141 (2013).
6. Miles, C. *et al.* Biventricular Myocardial Fibrosis and Sudden Death in Patients With Brugada Syndrome. *J. Am. Coll. Cardiol.* **78**, 1511–1521 (2021).
7. Chen, Q. *et al.* Genetic basis and molecular mechanism for idiopathic ventricular fibrillation. *Nature* **392**, 293–296 (1998).
8. Le Scouarnec, S. *et al.* Testing the burden of rare variation in arrhythmia-susceptibility genes provides new insights into molecular diagnosis for Brugada syndrome. *Hum. Mol. Genet.* **24**, 2757–2763 (2015).
9. Hosseini, S. M. *et al.* Reappraisal of Reported Genes for Sudden Arrhythmic Death: Evidence-Based Evaluation of Gene Validity for Brugada Syndrome. *Circulation* **138**, 1195 (2018).

715 10. Barc, J. *et al.* Genome-wide association analyses identify new Brugada syndrome risk loci
716 and highlight a new mechanism of sodium channel regulation in disease susceptibility. *Nat.*
717 *Genet.* 1–8 (2022) doi:10.1038/s41588-021-01007-6.
718 11. Bezzina, C. R. *et al.* Common variants at SCN5A-SCN10A and HEY2 are associated with
719 Brugada syndrome, a rare disease with high risk of sudden cardiac death. *Nat. Genet.* **45**,
720 1044–1049 (2013).
721 12. Deplancke, B., Alpern, D. & Gardeux, V. The Genetics of Transcription Factor DNA Binding
722 Variation. *Cell* **166**, 538–554 (2016).
723 13. Maurano, M. T. *et al.* Systematic localization of common disease-associated variation in
724 regulatory DNA. *Science* **337**, 1190–5 (2012).
725 14. Schaub, M. A., Boyle, A. P., Kundaje, A., Batzoglou, S. & Snyder, M. Linking disease
726 associations with regulatory information in the human genome. *Genome Res.* **22**, 1748–59
727 (2012).
728 15. Zhou, B. *et al.* Epicardial progenitors contribute to the cardiomyocyte lineage in the
729 developing heart. *Nature* **454**, 109–113 (2008).
730 16. Wessels, A. *et al.* Epicardially derived fibroblasts preferentially contribute to the parietal
731 leaflets of the atrioventricular valves in the murine heart. *Dev. Biol.* **366**, 111–124 (2012).
732 17. Duim, S. N., Goumans, M.-J. & Kruithof, B. P. T. WT1 in Cardiac Development and Disease.
733 in *Wilms Tumor* (ed. van den Heuvel-Eibrink, M. M.) (Codon Publications, Brisbane (AU),
734 2016).
735 18. Wagner, N. *et al.* Implications of the Wilms' Tumor Suppressor Wt1 in Cardiomyocyte
736 Differentiation. *Int. J. Mol. Sci.* **22**, 4346 (2021).
737 19. Tyser, R. C. V. *et al.* Characterization of a common progenitor pool of the epicardium and
738 myocardium. *Science* **371**, eabb2986 (2021).

739 20. Díaz del Moral, S. *et al.* Deletion of the Wilms' Tumor Suppressor Gene in the Cardiac
740 Troponin-T Lineage Reveals Novel Functions of WT1 in Heart Development. *Front. Cell*
741 *Dev. Biol.* **9**, (2021).
742 21. van Wijk, B., Gunst, Q. D., Moorman, A. F. M. & van den Hoff, M. J. B. Cardiac
743 Regeneration from Activated Epicardium. *PLoS ONE* **7**, e44692 (2012).
744 22. Zhou, B. *et al.* Adult mouse epicardium modulates myocardial injury by secreting paracrine
745 factors. *J. Clin. Invest.* **121**, 1894–1904 (2011).
746 23. Wagner, K.-D. *et al.* The Wilms' tumor suppressor Wt1 is expressed in the coronary
747 vasculature after myocardial infarction. *FASEB J.* **16**, 1117–1119 (2002).
748 24. Braitsch, C. M., Kanisicak, O., van Berlo, J. H., Molkentin, J. D. & Yutzey, K. E. Differential
749 expression of embryonic epicardial progenitor markers and localization of cardiac fibrosis in
750 adult ischemic injury and hypertensive heart disease. *J. Mol. Cell. Cardiol.* **65**,
751 10.1016/j.yjmcc.2013.10.005 (2013).
752 25. Hill, M. C. *et al.* Integrated multiomic characterization of congenital heart disease. *Nature* 1–
753 3 (2022) doi:10.1038/s41586-022-04989-3.
754 26. Reichart, D. *et al.* Pathogenic variants damage cell composition and single cell transcription
755 in cardiomyopathies. *Science* **377**, eabo1984 (2022).
756 27. Chaffin, M. *et al.* Single-nucleus profiling of human dilated and hypertrophic
757 cardiomyopathy. *Nature* **608**, 174–180 (2022).
758 28. Díaz del Moral, S. *et al.* Cardiomyocyte-Specific Wt1 Is Involved in Cardiac Metabolism and
759 Response to Damage. *J. Cardiovasc. Dev. Dis.* **10**, 211 (2023).
760 29. Mi, H., Muruganujan, A., Ebert, D., Huang, X. & Thomas, P. D. PANTHER version 14: more
761 genomes, a new PANTHER GO-slim and improvements in enrichment analysis tools.
762 *Nucleic Acids Res.* **47**, D419–D426 (2019).

763 30. Boukens, B. J., Walton, R., Meijborg, V. M. & Coronel, R. Transmural electrophysiological
764 heterogeneity, the T-wave and ventricular arrhythmias. *Prog. Biophys. Mol. Biol.* **122**, 202–
765 214 (2016).
766 31. Veerman, C. C. *et al.* The Brugada Syndrome Susceptibility Gene HEY2 Modulates Cardiac
767 Transmural Ion Channel Patterning and Electrical Heterogeneity. *Circ. Res.* **121**, 537–548
768 (2017).
769 32. Flurkey, K., M. Currer, J. & Harrison, D. E. Chapter 20 - Mouse Models in Aging Research.
770 in *The Mouse in Biomedical Research (Second Edition)* (eds. Fox, J. G. et al.) 637–672
771 (Academic Press, Burlington, 2007). doi:10.1016/B978-012369454-6/50074-1.
772 33. Shaw, R. M. & Rudy, Y. Ionic Mechanisms of Propagation in Cardiac Tissue. *Circ. Res.* **81**,
773 727–741 (1997).
774 34. Kohela, A. *et al.* Epicardial differentiation drives fibro-fatty remodeling in arrhythmogenic
775 cardiomyopathy. *Sci. Transl. Med.* **13**, eabf2750 (2021).
776 35. Muzumdar, M. D., Tasic, B., Miyamichi, K., Li, L. & Luo, L. A global double-fluorescent Cre
777 reporter mouse. *Genes. N. Y. N 2000* **45**, 593–605 (2007).
778 36. Protze, S. I. *et al.* Sinoatrial node cardiomyocytes derived from human pluripotent cells
779 function as a biological pacemaker. *Nat. Biotechnol.* **35**, 56–68 (2017).
780 37. Davis, C. A. *et al.* The Encyclopedia of DNA elements (ENCODE): data portal update.
781 *Nucleic Acids Res.* **46**, D794–D801 (2018).
782 38. Van Duijvenboden, K., De Boer, B. A., Capon, N., Ruijter, J. M. & Christoffels, V. M.
783 EMERGE: A flexible modelling framework to predict genomic regulatory elements from
784 genomic signatures. *Nucleic Acids Res.* **44**, (2015).
785 39. van Ouwerkerk, A. F. *et al.* Identification of atrial fibrillation associated genes and functional
786 non-coding variants. *Nat. Commun.* **10**, (2019).

787 40. Fernandez-Perez, A. *et al.* Hand2 Selectively Reorganizes Chromatin Accessibility to
788 Induce Pacemaker-like Transcriptional Reprogramming. *Cell Rep.* (2019)
789 doi:10.1016/j.celrep.2019.04.077.
790 41. van Duijvenboden, K. *et al.* Conserved NPPB+ Border Zone Switches From MEF2- to AP-1-
791 Driven Gene Program. *Circulation* **140**, 864–879 (2019).
792 42. Gilsbach, R. *et al.* Distinct epigenetic programs regulate cardiac myocyte development and
793 disease in the human heart in vivo. *Nat. Commun.* **9**, (2018).
794 43. Feyen, D. A. M. *et al.* Metabolic Maturation Media Improve Physiological Function of Human
795 iPSC-Derived Cardiomyocytes. *Cell Rep.* **32**, 107925 (2020).
796 44. Verkerk, A. O. & Wilders, R. Injection of IK1 through dynamic clamp can make all the
797 difference in patch-clamp studies on hiPSC-derived cardiomyocytes. *Front. Physiol.* **14**,
798 1326160 (2023).
799 45. Man, J. C. K. *et al.* An enhancer cluster controls gene activity and topology of the SCN5A-
800 SCN10A locus in vivo. *Nat. Commun.* **10**, 4943 (2019).
801 46. Marchal, G. A. *et al.* Genetic background determines the severity of age-dependent cardiac
802 structural abnormalities and arrhythmia susceptibility in Scn5a-1798insD mice. *Eur. Eur.*
803 *Pacing Arrhythm. Card. Electrophysiol. J. Work. Groups Card. Pacing Arrhythm. Card. Cell.*
804 *Electrophysiol. Eur. Soc. Cardiol.* **26**, euae153 (2024).
805 47. Xing, S. *et al.* Genetic influence on electrocardiogram time intervals and heart rate in aging
806 mice. *Am. J. Physiol. - Heart Circ. Physiol.* **296**, H1907 (2009).
807 48. de Wit, E. *et al.* CTCF Binding Polarity Determines Chromatin Looping. *Mol. Cell* **60**, 676–
808 684 (2015).
809 49. Dixon, J. R. *et al.* Topological domains in mammalian genomes identified by analysis of
810 chromatin interactions. *Nature* **485**, 376–80 (2012).
811 50. Nora, E. P. *et al.* Spatial partitioning of the regulatory landscape of the X-inactivation centre.
812 *Nature* **485**, 381–385 (2012).

813 51. Toska, E. & Roberts, S. G. E. Mechanisms of transcriptional regulation by WT1 (Wilms'
814 tumour 1). *Biochem. J.* **461**, 15–32 (2014).
815 52. Rampal, R. *et al.* DNA Hydroxymethylation Profiling Reveals that WT1 Mutations Result in
816 Loss of TET2 Function in Acute Myeloid Leukemia. *Cell Rep.* **9**, 1841–1855 (2014).
817 53. Wang, Y. *et al.* WT1 Recruits TET2 to Regulate Its Target Gene Expression and Suppress
818 Leukemia Cell Proliferation. *Mol. Cell* **57**, 662–673 (2015).
819 54. Essafi, A. *et al.* A Wt1-Controlled Chromatin Switching Mechanism Underpins Tissue-
820 Specific Wnt4 Activation and Repression. *Dev. Cell* **21**, 559–574 (2011).
821 55. Larsson, S. H. *et al.* Subnuclear localization of WT1 in splicing or transcription factor
822 domains is regulated by alternative splicing. *Cell* **81**, 391–401 (1995).
823 56. Shandilya, J., Toska, E., Richard, D. J., Medler, K. F. & Roberts, S. G. E. WT1 interacts with
824 MAD2 and regulates mitotic checkpoint function. *Nat. Commun.* **5**, 4903 (2014).
825 57. von Gise, A. *et al.* WT1 regulates epicardial epithelial to mesenchymal transition through β-
826 catenin and retinoic acid signaling pathways. *Dev. Biol.* **356**, 421–431 (2011).
827 58. Bergmann, O. & Jovinge, S. Isolation of Cardiomyocyte Nuclei from Post-mortem Tissue. *J.*
828 *Vis. Exp. JoVE* 4–9 (2012) doi:10.3791/4205.
829 59. Dobin, A. *et al.* STAR: Ultrafast universal RNA-seq aligner. *Bioinformatics* **29**, 15–21 (2013).
830 60. Ruijter, J. M. *et al.* Amplification efficiency: Linking baseline and bias in the analysis of
831 quantitative PCR data. *Nucleic Acids Res.* **37**, (2009).
832 61. Doshi, A. N. *et al.* Feasibility of a semi-automated method for cardiac conduction velocity
833 analysis of high-resolution activation maps. *Comput. Biol. Med.* **65**, 177–183 (2015).
834 62. ten Hoope, W. *et al.* Pharmacodynamics and Pharmacokinetics of Lidocaine in a Rodent
835 Model of Diabetic Neuropathy. *Anesthesiology* **128**, 609 (2018).
836 63. Veerman, C. C. *et al.* hiPSC-derived cardiomyocytes from Brugada Syndrome patients
837 without identified mutations do not exhibit clear cellular electrophysiological abnormalities.
838 *Sci. Rep.* **6**, 30967 (2016).

839 64. Verkerk, A. O. & Wilders, R. Dynamic Clamp in Electrophysiological Studies on Stem Cell–
840 Derived Cardiomyocytes—Why and How? *J. Cardiovasc. Pharmacol.* **77**, 267 (2021).
841 65. Meijer van Putten, R. M. E. *et al.* Ion channelopathies in human induced pluripotent stem
842 cell derived cardiomyocytes: a dynamic clamp study with virtual IK1. *Front. Physiol.* **6**,
843 (2015).
844 66. Hobai, I. A., Bates, J. A., Howarth, F. C. & Levi, A. J. Inhibition by external Cd2+ of Na/Ca
845 exchange and L-type Ca channel in rabbit ventricular myocytes. *Am. J. Physiol.-Heart Circ.*
846 *Physiol.* **272**, H2164–H2172 (1997).
847 67. Sheets, M. F. & Hanck, D. A. Mechanisms of extracellular divalent and trivalent cation block
848 of the sodium current in canine cardiac Purkinje cells. *J. Physiol.* **454**, 299–320 (1992).
849 68. Ackers-Johnson, M. *et al.* A Simplified, Langendorff-Free Method for Concomitant Isolation
850 of Viable Cardiac Myocytes and Nonmyocytes From the Adult Mouse Heart. *Circ. Res.* **119**,
851 909 (2016).
852

853

Acknowledgements

We acknowledge the resources and support from the Core Facility Genomics of the Amsterdam UMC for the RNA sequencing experiments. We are thankful to Jaël Copier, Caroline Pham, and Aya Aliawi for their technical assistance. We thank Vincent Christoffels for insightful discussions which were helpful in the advancement of this work.

Figure 1

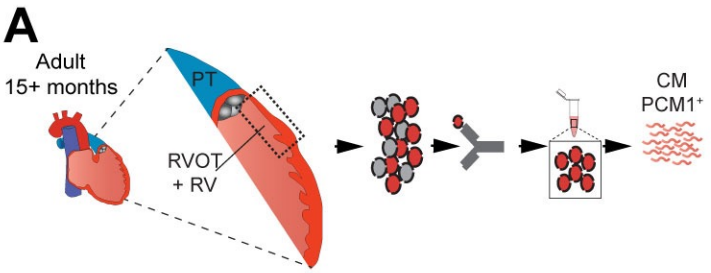

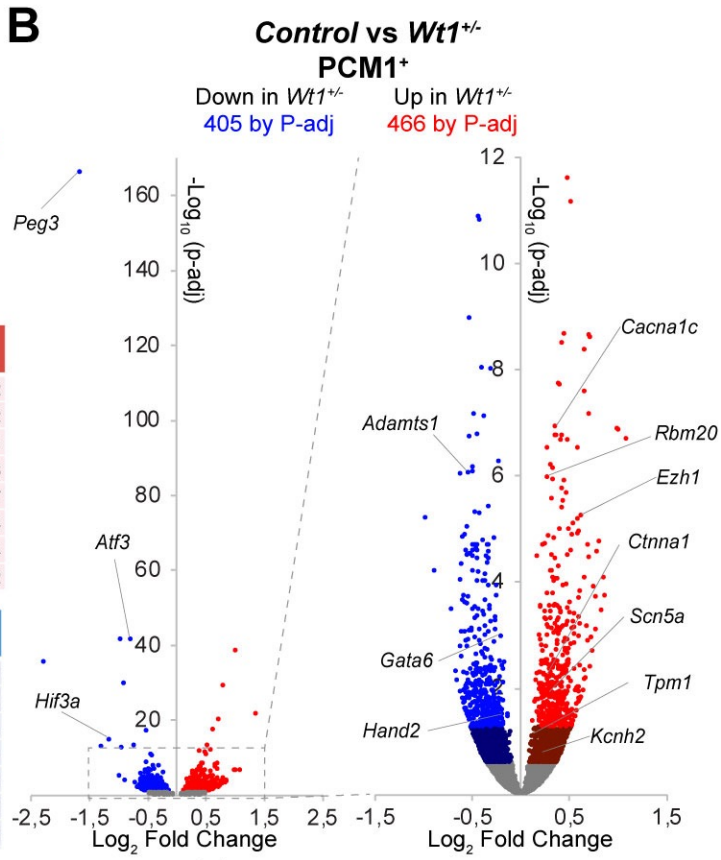

C

GO biological process upregulated in *Wt1*+/- CM	Fold Enrichment	Raw P-value	FDR
cellular component organization (GO:0016043)	1.75	1.31E-15	4.14E-12
developmental process (GO:0032502)	1.71	1.89E-15	4.97E-12
regulation of cell communication (GO:0010646)	2.02	7.85E-15	1.03E-11
cell differentiation (GO:0030154)	1.78	1.35E-10	6.43E-08
regulation of gene expression (GO:0010468)	1.62	9.85E-10	3.98E-07
regulation of cardiac muscle contraction (GO:0055117)	7.61	2.09E-06	2.59E-04
regulation of transport (GO:0051049)	1.84	2.55E-06	3.04E-04
cell motility (GO:0048870)	1.90	2.30E-04	1.25E-02

GO biological process downregulated in *Wt1*+/- CM	Fold Enrichment	Raw P-value	FDR
cellular respiration (GO:0045333)	6.67	3.63E-10	1.43E-06
metabolic process (GO:0008152)	1.41	1.66E-08	3.73E-05
cellular localization (GO:0051641)	1.81	2.34E-07	3.35E-04
muscle tissue development (GO:0060537)	3.59	9.88E-07	1.04E-03
intracellular transport (GO:0046907)	1.99	3.86E-05	1.17E-02
electron transport chain (GO:0022900)	5.67	5.42E-05	1.50E-02
apoptotic process (GO:0006915)	2.07	1.47E-04	2.61E-02

D

Kcnip2	3,1E-05
Cacna1s	0,00881
Clcn7	0,04144
Kcnq1	0,00109
Chrna10	0,01176
Cacna1c	1,6E-07
Abcc8	0,00025
Itpr2	1,1E-06
Scn5a	0,01242
Ryr2	3E-05
Atp1b3	0,01465
Slc22a4	0,0014
Kcnh7	0,03188

1.8
-2.4

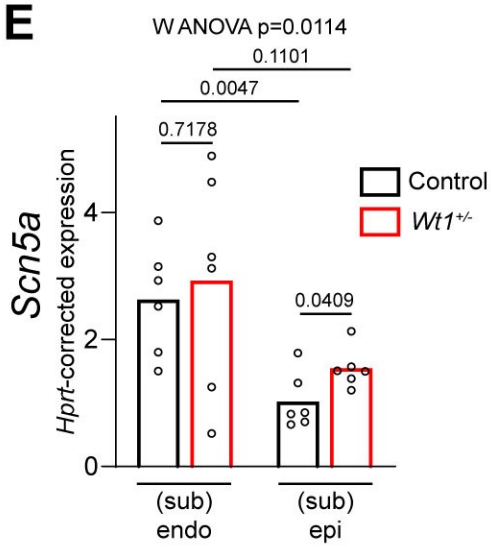

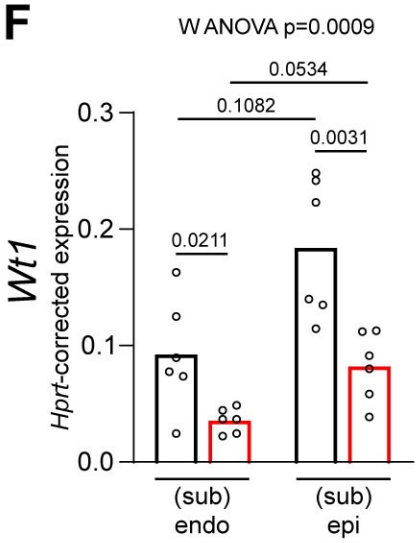

Figure 2

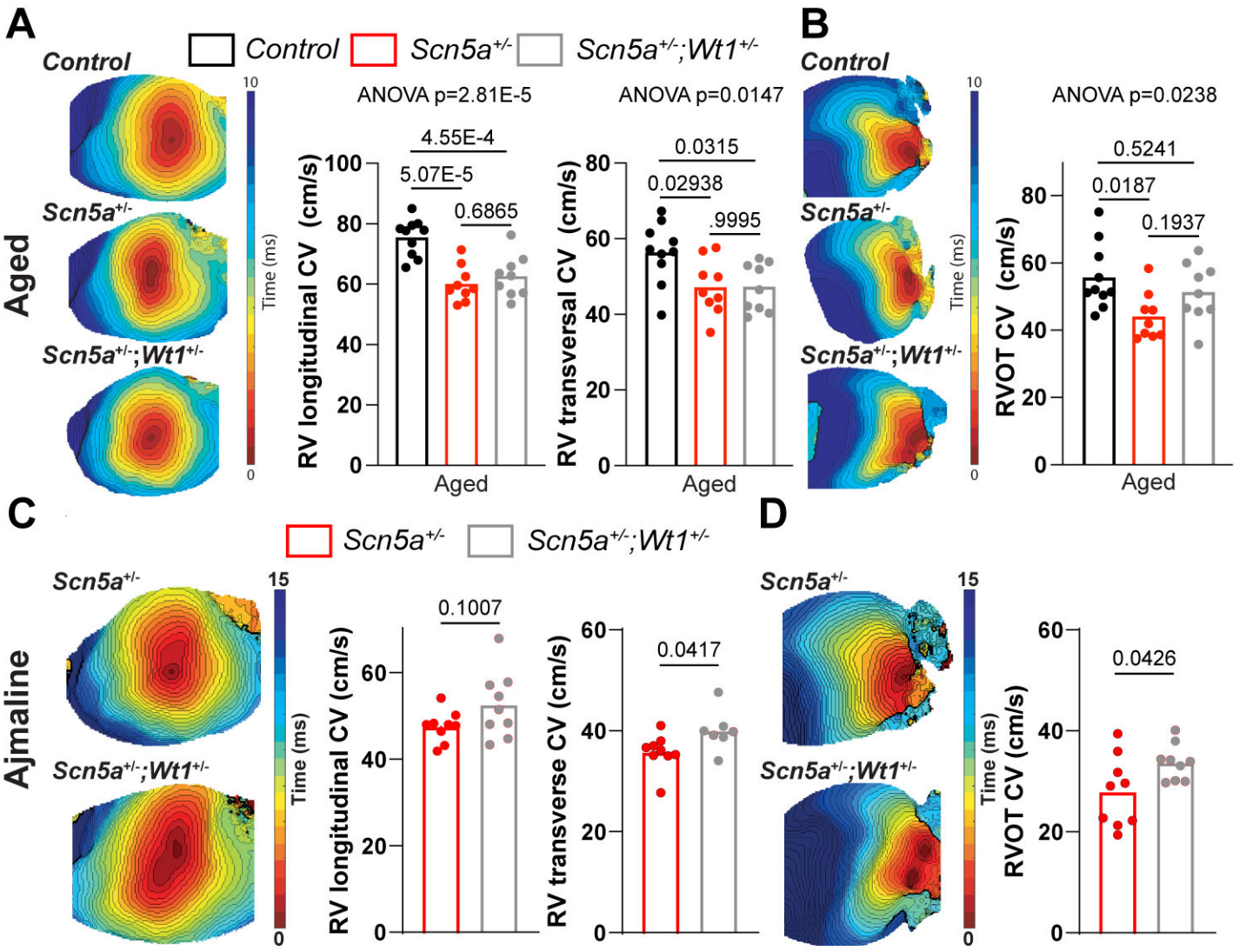
A
Control
Scn5a+/-
Scn5a+/-;Wt1+/-
Aged
Time (ms)
10
0
ANOVA p=2.81E-5
4.55E-4
5.07E-5
0.6865
RV longitudinal CV (cm/s)
Aged
ANOVA p=0.0147
0.0315
0.02938
.9995
RV transversal CV (cm/s)
Aged
B
Control
Scn5a+/-
Scn5a+/-;Wt1+/-
Time (ms)
ANOVA p=0.0238
0.5241
0.0187
0.1937
RVOT CV (cm/s)
Aged
C
Scn5a+/-
Scn5a+/-;Wt1+/-
Ajmaline
Time (ms)
15
0
0.1007
RV longitudinal CV (cm/s)
0.0417
RV transverse CV (cm/s)
D
Scn5a+/-
Scn5a+/-;Wt1+/-
Time (ms)
0.0426
RVOT CV (cm/s)

Figure 3

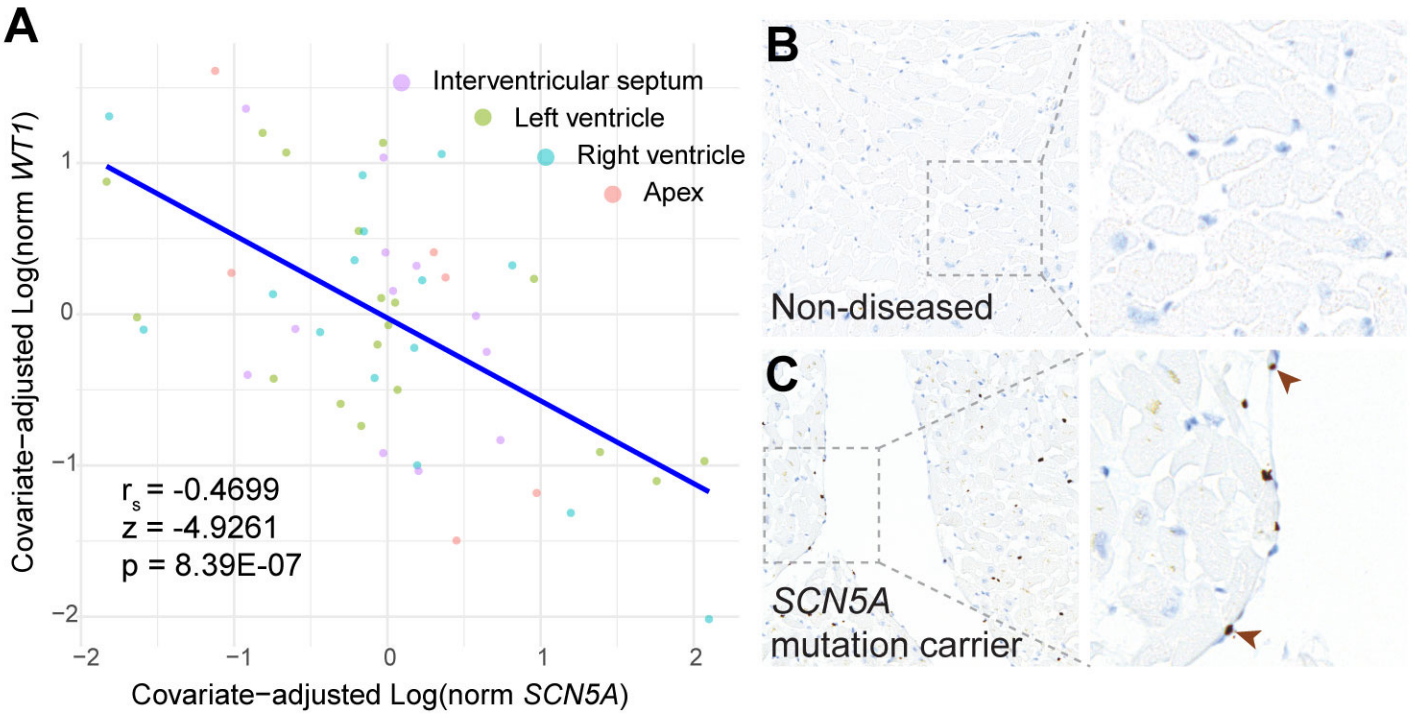
A
Interventricular septum
Left ventricle
Right ventricle
Apex
r_s = -0.4699
z = -4.9261
p = 8.39E-07
Covariate−adjusted Log(norm *WT1*)
Covariate−adjusted Log(norm *SCN5A*)
1
0
−1
−2
−2
−1
0
1
2
B
Non-diseased
C
SCN5A
mutation carrier

Figure 4

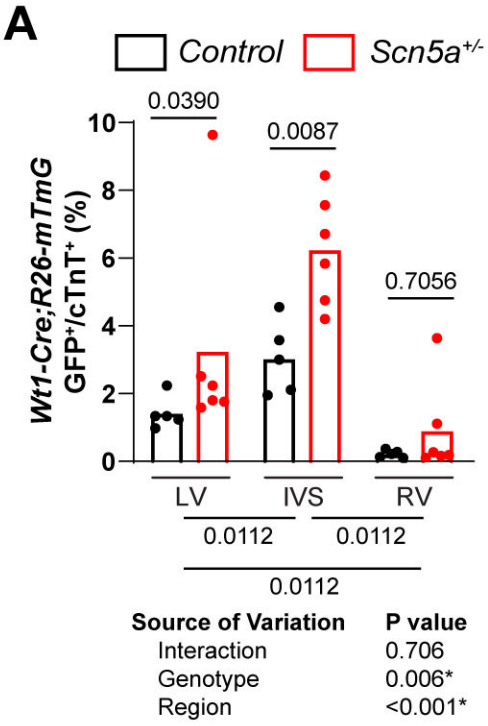
A
Control
Scn5a+/-
Wt1-Cre;R26-mTmG GFP+/cTnT+ (%)
10
8
6
4
2
0
0.0390
0.0087
0.7056
LV
IVS
RV
0.0112
0.0112
0.0112
Source of Variation
P value
Interaction
0.706
Genotype
0.006*
Region
<0.001*

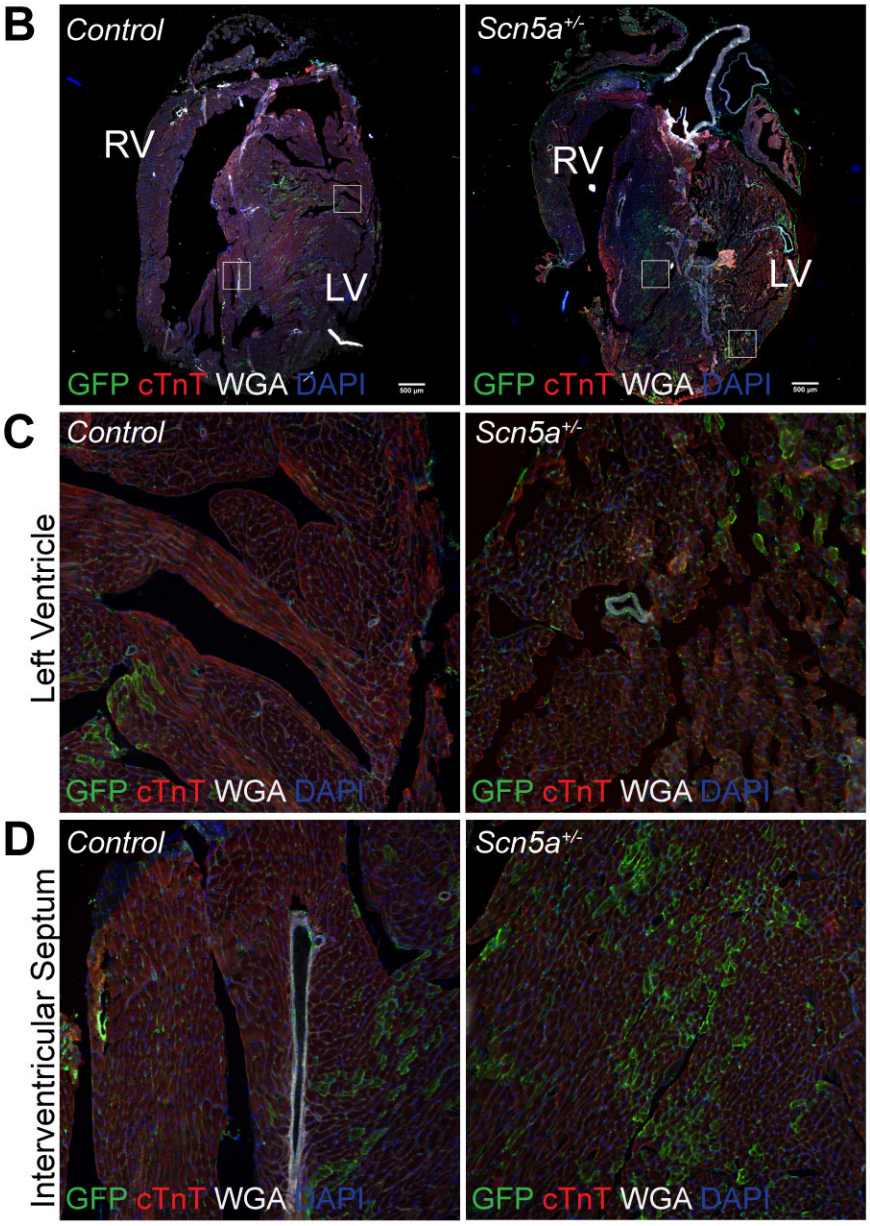
B
Control
Scn5a+/-
RV
LV
GFP cTnT WGA DAPI
C
Left Ventricle
D
Interventricular Septum

Figure 5

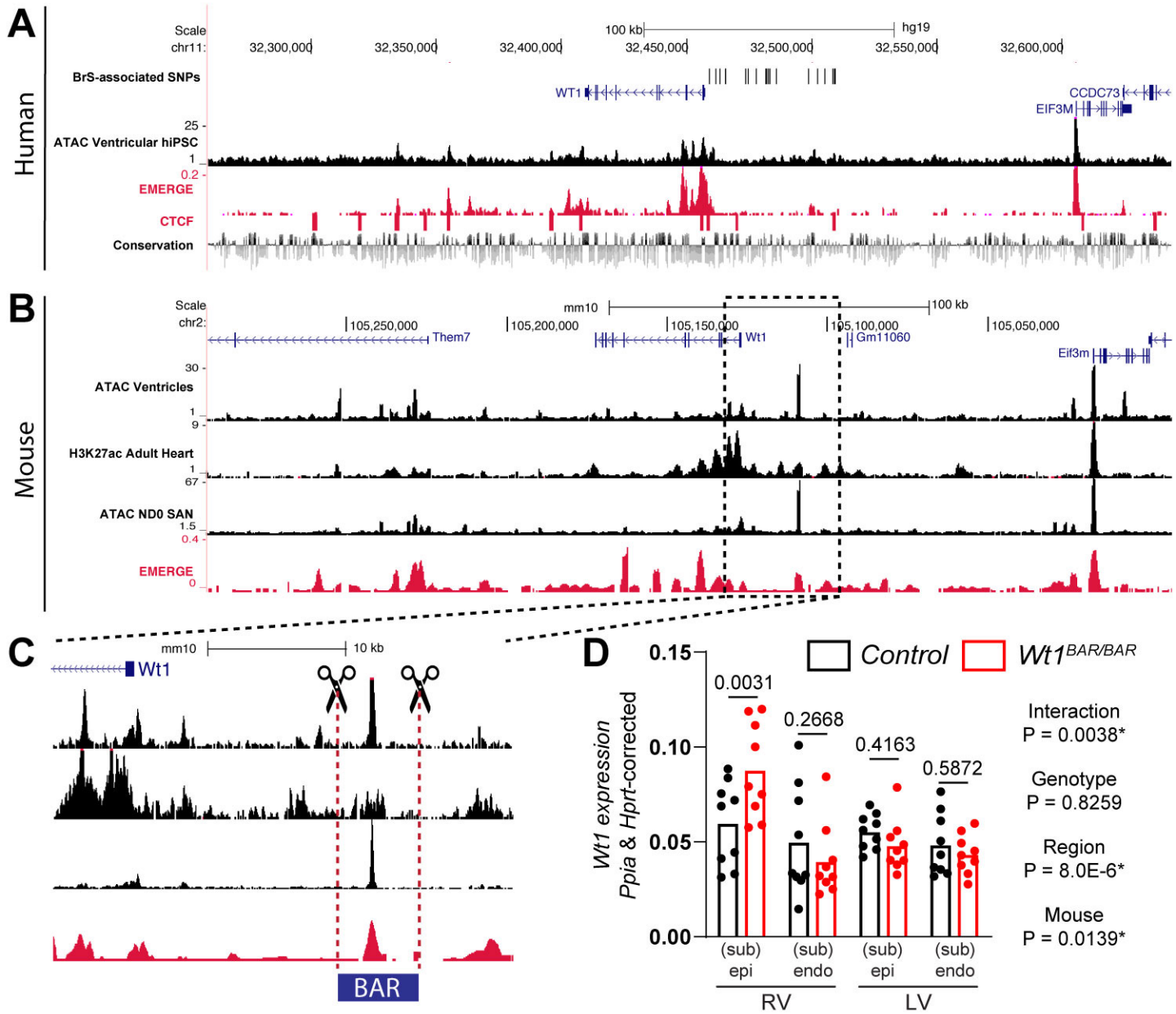
A
Human
Scale
chr11:
100 kb
hg19
32,300,000
32,350,000
32,400,000
32,450,000
32,500,000
32,550,000
32,600,000
BrS-associated SNPs
WT1
CCDC73
EIF3M
ATAC Ventricular hiPSC
EMERGE
CTCF
Conservation
B
Mouse
Scale
chr2:
mm10
100 kb
105,250,000
105,200,000
105,150,000
105,100,000
105,050,000
Them7
Wt1
Gm11060
Eif3m
ATAC Ventricles
H3K27ac Adult Heart
ATAC ND0 SAN
EMERGE
C
mm10
10 kb
Wt1
BAR
D
Control
Wt1BAR/BAR
Wt1 expression
Ppia & Hprt-corrected
0.15
0.10
0.05
0.00
0.0031
0.2668
0.4163
0.5872
(sub) epi
(sub) endo
(sub) epi
(sub) endo
RV
LV
Interaction
P = 0.0038*
Genotype
P = 0.8259
Region
P = 8.0E-6*
Mouse
P = 0.0139*

Figure 6

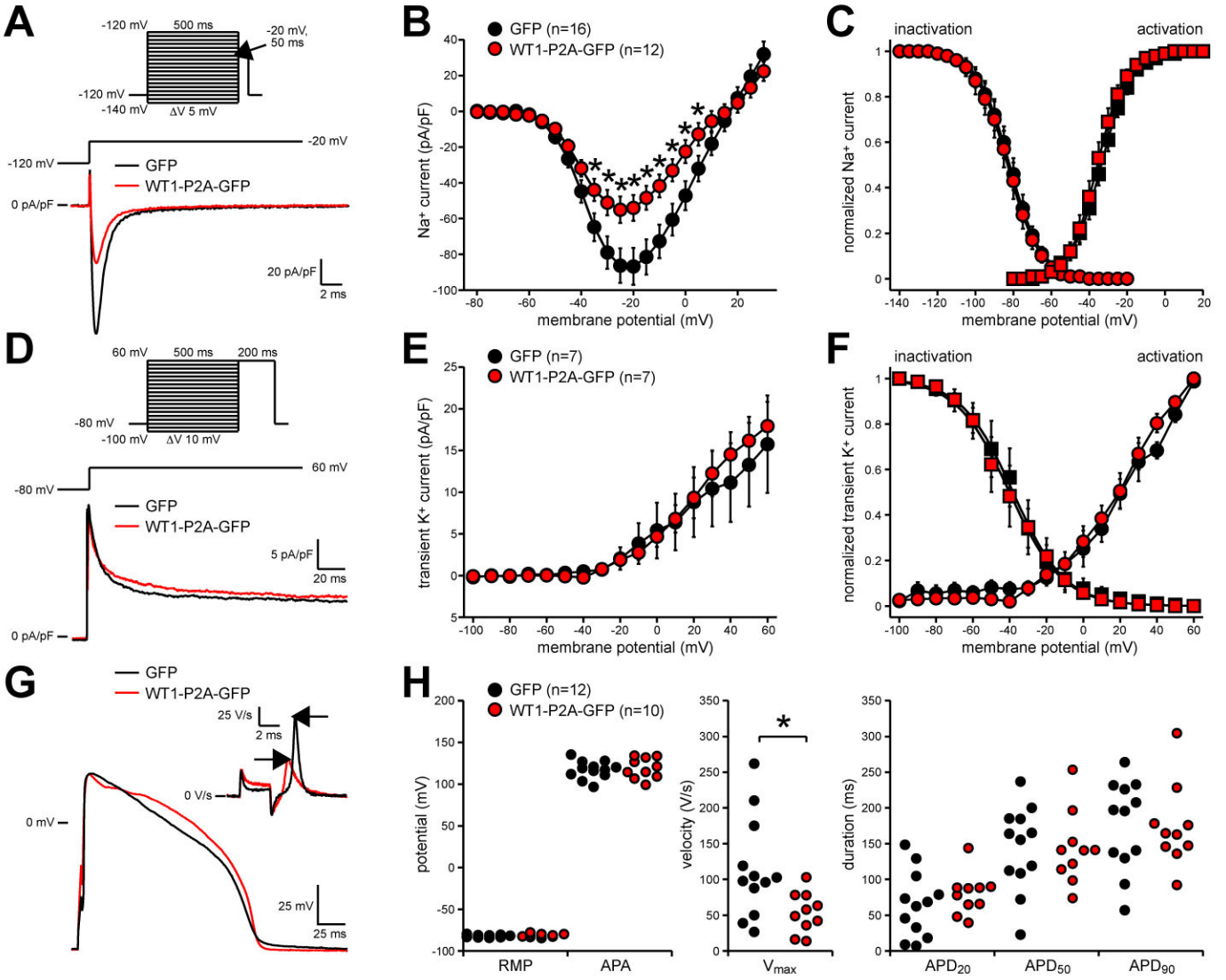
A
-120 mV
500 ms
-20 mV, 50 ms
-120 mV
-140 mV
ΔV 5 mV
-20 mV
-120 mV
GFP
WT1-P2A-GFP
0 pA/pF
20 pA/pF
2 ms
B
GFP (n=16)
WT1-P2A-GFP (n=12)
Na+ current (pA/pF)
membrane potential (mV)
C
inactivation
activation
normalized Na+ current
membrane potential (mV)
D
60 mV
500 ms
200 ms
-80 mV
-100 mV
ΔV 10 mV
60 mV
-80 mV
GFP
WT1-P2A-GFP
5 pA/pF
20 ms
0 pA/pF
E
GFP (n=7)
WT1-P2A-GFP (n=7)
transient K+ current (pA/pF)
membrane potential (mV)
F
inactivation
activation
normalized transient K+ current
membrane potential (mV)
G
GFP
WT1-P2A-GFP
25 V/s
2 ms
0 V/s
0 mV
25 mV
25 ms
H
GFP (n=12)
WT1-P2A-GFP (n=10)
potential (mV)
RMP
APA
velocity (V/s)
Vmax
duration (ms)
APD20
APD50
APD90